

# One-dimensional behavior of elongated Bose-Einstein condensates

P. Bouyer<sup>1</sup>, J. H. Thywissen<sup>2</sup>, F. Gerbier<sup>1</sup>, M. Hugbart<sup>1</sup>, S. Richard<sup>1</sup>, J. Retter<sup>1</sup> and A. Aspect<sup>1</sup>

<sup>1</sup> *Laboratoire Charles Fabry de l'Institut d'Optique, UMR 8501 du CNRS, 91403 Orsay Cedex, France*

<sup>2</sup> *Department of Physics, 60 St George Street, University of Toronto, Toronto, ON, M5S 1A7, Canada*

## Abstract

We study the properties of elongated Bose-Einstein condensates. First, we show that the dimensions of the condensate after expansion differs from the 3D Thomas-Fermi regime. We also study the coherence length of such elongated condensates.

## 1 INTRODUCTION

The experimental study of one dimensional (1D) degenerate Bose gases, where the radial motion is “frozen”, is currently an important direction of research in ultra-cold atom physics [1,2,3]. In uniform 1D systems, fluctuations of the condensate phase are pronounced, because of a large population of low-lying states; as a result, no long range order exists at any temperature. In a trapped 1D gas, the finite size of the sample naturally introduces a low-energy cutoff, and at sufficiently low temperature a phase coherent sample can exist (see [4] and references therein for the properties of 1D gases). Essentially, the same analysis holds for three dimensional (3D) trapped gases in very elongated traps [5]: here the interaction energy per particle is larger than the radial frequency, and the condensate wavefunction is built from several radial modes. Still, low-energy excitations with a frequency smaller than the radial frequency are effectively one-dimensional, and induce large fluctuations of the condensate phase [5]. Such condensates with a fluctuating phase, or *quasicondensates*, have been observed experimentally in [6,7,8,10,9].

We present here an overview of our experimental study of elongated condensates in a very anisotropic trap. Our set-up, presented in section 2 allows us to characterize precisely the properties of degenerate gases between the 3D and 1D regimes. In this regime, we first show (section 3) that the (quasi)condensates exhibit the same smooth profile as a true (fully coherent) condensate. This profile, however, is affected by both the radial quantum pressure (zero point oscillation in the tight trapping potential) and the presence of an interacting thermal cloud surrounding the condensate and interacting with it through two-body repulsive interactions. In section 4, we discuss the coherence length of such elongated condensates. Using Bragg spectroscopy [13,10,12,11], we show in section 4.1 that the coherence length is indeed strongly affected by large fluctuations of the condensate phase [5] and that the measured momentum width depends strongly on temperature; the corresponding coherence length  $L_\phi$ , in the ratio

$5 < \frac{L}{L_\phi} < 30$ , is in good agreement with theory [5,12]. For larger coherence length, Bragg spectroscopy becomes increasingly difficult to apply, and a second method, using a  $\pi/2 - \pi/2$  interferometer similar to [9] is presented in section 4.2.

## 2 CREATION OF ELONGATED BEC IN A IRON-CORE ELECTROMAGNET

The experimental setup has been described elsewhere [14]. Briefly, a Zeeman-slowed atomic beam of  $^{87}\text{Rb}$  is trapped in a MOT, and after optical pumping into the  $F = 1$  state is transferred to a magnetic Ioffe-Pritchard trap created by an iron-core electromagnet. A new design allows us to lower the bias field to a few Gauss and thus to obtain very tight radial confinement [15]. Final radial and axial trap frequencies ( $\omega_\perp$  and  $\omega_z$ ) are respectively 760 Hz and 5 Hz (i.e. aspect ratio = 152). In this way, we obtain needle-shaped condensates containing around  $5 \times 10^4$  atoms [16], with a typical half-length  $L \simeq 130 \mu\text{m}$  and radius  $R \simeq 0.8 \mu\text{m}$ . Since the chemical potential  $\frac{\mu_{\text{TF}}}{\hbar\omega_\perp} \sim 4$  (see definition in section 3), the clouds are between the 3D and 1D Thomas-Fermi (TF) regimes [1, 2, 3]. The measurement of the number of atoms is calibrated from a measurement of  $T_C$ . The temperature  $T$  is extracted from a two-component fit to the absorption images or is extrapolated from the final frequency of the rf ramp when the thermal fraction is indiscernible. After the last evaporation ramp, we observe the formation of a condensate that exhibits strong shape oscillations (see [17] and references therein). This is in line with a recent observation by Shvarchuck *et al.* [8], who propose the picture of a BEC locally in equilibrium at each point on the axis, but globally out of equilibrium. Indeed, the radial degrees of freedom are rapidly thermalized, but axial motion damps on a much longer time scale. We therefore hold the condensate for a variable time (typically 7 seconds) in presence of an rf shield, so that these collective oscillations have no influence on the Bragg spectra.

## 3 EXPANSION OF ELONGATED CONDENSATES

In anisotropic traps, the aspect ratio of the ballistically expanding cloud can be used to find a signature of Bose-Einstein Condensation. For a Bose gas above critical temperature, the expanding cloud is expected to become isotropic at long expansion times (typically for times larger than  $1/\omega_z$ , where  $\omega_z$  is the smaller trap oscillation frequency). On the contrary, a Bose-Einstein condensate of initial aspect ratio  $\epsilon = \omega_z/\omega_\perp$  will only become isotropic at a fixed time  $\sim \omega_z^{-1}$  and then will invert its anisotropy for longer expansion time.

The transition from a 3D to a lower dimension (1D) condensate is also observable through the expansion of the degenerate gas [1]. For a Bose-Einstein condensate in the 3D Thomas-Fermi regime ( $\mu \gg \hbar\omega_\perp$ ), the half-length  $L_{\text{TF}}$  (long axis) and the radius  $R_{\text{TF}}$  (confined dimension) of the condensate vary similarly with the number of atoms  $N_0$ . More precisely, one finds the 3D Thomas-Fermi length  $L_{\text{TF}}^2 = 2\mu/(M\omega_z^2)$  and radius  $R_{\text{TF}} = \epsilon L_{\text{TF}}$ , with  $\mu$  given by  $2\mu = \hbar\bar{\omega}(15N_0a/\sigma)^{2/5}$  [17], where  $\bar{\omega} = (\omega_\perp^2\omega_z)^{1/3}$ ,  $\sigma = \sqrt{\hbar/(M\bar{\omega})}$  and  $a = 5.32 \text{ nm}$  [18]. As a result, the initial degree of anisotropy  $\epsilon = R/L = \omega_z/\omega_\perp \ll 1$  is independent of the number of atoms. After a period of free expansion of duration  $t$ , the dimension of the expanding condensate are found using the scaling solutions [19]:

$$R(t) = R_{\text{TF}}\sqrt{1 + \tau^2}. \quad (3.1)$$

$$L(t) = L_{\text{TF}}(1 + \epsilon^2 \left[ \tau \arctan \tau - \ln \sqrt{1 + \tau^2} \right]) \simeq L_{\text{TF}}. \quad (3.2)$$

with the dimensionless time variable  $\tau = \omega_\perp t$ . Equations (3.1,3.2) show that the aspect ratio is independent of the atom number at any time, and approaches  $\omega t$  for  $\tau \gg 1$

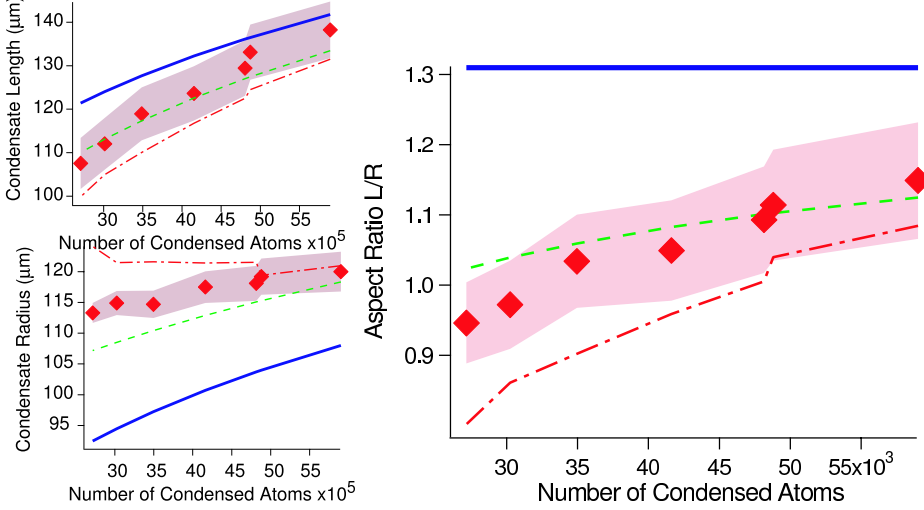


**Fig. 1.** Half-length  $L$  (upper-left), radius  $R$  (lower-left) and aspect ratio (right) of the quasi-1D condensate versus the condensed atom number after a 24.3 ms time of flight. Experimental values (diamonds) are compared to the standard  $T = 0$  Thomas-Fermi (plain), and the self consistent solution of equations (3.4) and (3.3) (dashed). The effect of quantum pressure alone is also shown (dot-dashed). Calculations use the measured temperature and number of condensed atoms, as determined by a two-component fit to averaged absorption images. Combined statistical and systematic errors are indicated with the confidence band (grayed area) around the experimental points.

As one pushes towards the 1D regime ( $\mu \sim \hbar\omega_{\perp}$ ), the radial expansion is increasingly affected by radial zero-point motion in the trap, neglected in the 3D TF approximation. Ultimately, the radial size in the trap should approach  $a_{\perp} = \sqrt{\hbar/M\omega_{\perp}}$ , and the radial expansion velocity  $\omega_{\perp}a_{\perp} = \sqrt{\hbar\omega_{\perp}/M}$ . Since axially the TF approximation ( $\mu \gg \hbar\omega_z$ ) is still valid, the length still depends on  $N_0$ , and so does the aspect ratio. Accordingly, a dependence of the aspect ratio on  $N_0$  at near-zero temperature can be seen as a signature of the breakdown of the TF approximation in the radial direction [1].

To show how quantum pressure manifests itself in our experiment, we first turn to the measurement of the axial half-length  $L$  after release, which faithfully reflects the half-length in the trap since axial expansion is negligible (eq. 3.2) for our experimental parameter. Figure 1 shows that the measured values of  $L$  for various number of condensed atoms (filled diamonds) are smaller than the standard Thomas-Fermi prediction (solid line). This smaller value results from radial quantum pressure (1D), and to a slightly larger extent from the compression of the quasi-condensate by the 3D thermal component (excitations with energy much larger than  $\hbar\omega_{\perp}$ ).

We take into account radial quantum pressure in this crossover regime by finding the optimal ground state energy [21]

$$\frac{E}{N} = \max_{\gamma_x, \gamma_y, \gamma_z} \left[ \sum_{i=1}^3 \frac{\hbar\omega_i}{2} \sqrt{\gamma_i} + \frac{5}{14} \left( \frac{15}{4\pi} g N m^{3/2} \prod_{i=1}^3 (\sqrt{1 - \gamma_i \omega_i}) \right)^{2/5} \right]. \quad (3.3)$$

where  $\gamma_i$  are effective parameters taking the zero-point energy contribution in the direction  $i = \{x, y, z\}$  into account. Solving (eq. 3.3) allows then to calculate a modified aspect ratio in the trap  $\tilde{\epsilon} = \gamma_z/\gamma_{x,y}$ . To include the effect of the thermal cloud, we use the Hartree-Fock

approach [20, 17] and calculate the modified length :

$$L^2 = \frac{2g}{M\omega_z^2} \left\{ n_0(0) + \frac{2}{\lambda_T^3} \left[ g_{3/2}(e^{-\frac{gn_0(0)}{k_B T}}) - g_{3/2}(1) \right] \right\}, \quad (3.4)$$

with the coupling constant  $g = 4\pi\hbar^2 a/M$ , the thermal de Broglie wavelength  $\lambda_T = [2\pi\hbar^2/(Mk_B T)]^{1/2}$ , and  $g_{3/2}(x) = \sum_{n=1}^{\infty} x^n/n^{3/2}$ . The black dashed line in Fig. 1 shows the solution of Eq. (3.4) assuming a parabolic profile, such that  $n_0(0) = 15N_0 L^{-3}\tilde{\epsilon}^2/(8\pi)$ . The modified aspect ratio in the trap  $\tilde{\epsilon}$  is calculated according to 3.3 and by a self-consistent iteration of equations (3.4) and (3.3) we obtain  $L$  and  $\gamma_{x,y,z}$ . We find that the calculated lengths are close to our measurements to within our estimated calibration uncertainty (shown by the grayed area explained in the caption).

We then turn to the measurement of the cloud radius after 24.3 ms of time of flight. Figure 1 shows that the measured values of  $R$  at various condensed atom number (filled diamonds) are larger by about 20% than the standard Thomas-Fermi prediction (filled line). This increased radius results again from quantum pressure, which leads to an excess released energy in the transverse direction. Using again [21], the radius after time of flight is found to be:

$$R(t)^2 = R_{\text{TF}}^2 \frac{\prod_{i=1}^3 (1 - \gamma_i)^{\frac{1}{5}}}{\sqrt{1 - \gamma_{x,y}}} (1 + \tau^2), \quad (3.5)$$

with  $\gamma_i$  calculated from (eq. 3.3). Calculating the effect of the compression of the thermal cloud and the subsequent evolution in time of flight is more complex, since it involves energy exchange between both components. By making the extreme assumption that all the interaction energy is converted to kinetic energy into the condensate after expansion, we can use again equation 3.5 with correction from 3.4 and 3.3. The results presented in figure 1 show that, both approaches agree with the experiment to within our calibration errors.

Finally, we observe a clear dependence of the aspect ratio on the condensed atom number, which can be correctly reproduced by our theoretical approach. This proves that in our trap, with this atom number ( $\sim 5 \times 10^4$ ), the condensate is at the onset of 1D.

#### 4 MEASUREMENT OF THE 1D PHASE FLUCTUATIONS

Phase coherence of the (quasi)condensate can be characterized by the  $1/e$  decay length of the spatial correlation function,  $\mathcal{C}^{(1)}(s) = 1/N \int d^3\mathbf{R} \langle \hat{\Psi}^\dagger(\mathbf{R} + s\mathbf{e}_z/2) \hat{\Psi}(\mathbf{R} - s\mathbf{e}_z/2) \rangle$  [27], with  $\hat{\Psi}$  the atomic field operator and  $\mathbf{e}_z$  the unit vector in the axial direction. Consider a sample of  $N_0$  condensed atoms, trapped in a cylindrically symmetric, harmonic trap with an aspect ratio  $\lambda = \omega_z/\omega_\perp \ll 1$ , in the 3D Thomas-Fermi regime. Petrov *et al.* [4, 5] investigated the long wavelength fluctuations of the phase of  $\Psi$ , with the following conclusions. Below a characteristic temperature  $T_\phi = 15N_0(\hbar\omega_z)^2/32\mu$ , the phase fluctuations are small, and the coherence length is essentially the condensate size  $L$ , as in “ordinary” 3D condensates [13, 22] (to put it differently,  $\mathcal{C}^{(1)}$  is limited by the density envelope of  $\Psi$ ). On the other hand, for  $T \gg T_\phi$  the coherence length is limited to a value much smaller than  $L$ , the value at the center of the trap being  $L_\phi = LT_\phi/T$ .

The theoretical results obtained in [5, 12] do not apply directly to our experiment. In those works, a 3D Thomas-Fermi density profile was assumed, whereas in our case modification of the density profile by the thermal cloud and radial quantum pressure must be accounted for. As discussed in the previous section, we indeed find that a parabolic profile is still a good fit function, but that the usual  $T = 0$  relations between  $\mu$ ,  $L$ ,  $R$ , and the number of condensed atoms  $N_0$  are no longer valid. We therefore extend the calculation of the axial correlation

function in [12] to an arbitrary density profile, in the local density approximation. In the mean field regime [4], from the result of [23] for a 1D uniform Bose gas at finite temperature, we obtain:

$$C(s) = \int dz n_1(z) \exp\left(-\frac{n_1(0)|s|}{2n_1(z)L_\phi}\right), \quad (4.1)$$

where  $n_1(z) = \int d^2\mathbf{r}_\perp n_0(\mathbf{r}_\perp, z)$  is the axial 1D density of the quasi-condensate, while  $n_0(\mathbf{r})$  is its 3D density profile. The coherence length near the center of the trap is given by  $L_\phi = \hbar^2 n_1(0)/(Mk_B T)$  [24]. Following Petrov *et al.* [4,5], we define the temperature which delineates the border between coherent and phase-fluctuating condensates as  $T_\phi = L_\phi T/L$ . Since  $n_1(0)$ ,  $L$ , and  $T$  are extracted directly from the images, the definitions of  $L_\phi$  and  $T_\phi$  relate the coherence properties to experimentally measured quantities. The axial momentum distribution follows from a Fourier transform of  $C(s)$  and is well approximated by a Lorentzian of width  $\Delta p_\phi = \alpha \hbar/L_\phi$  (HWHM), with  $\alpha = 0.67$  for a 3D Thomas-Fermi condensate [12,25].

#### 4.1 Momentum spectroscopy with Bragg diffraction

A convenient technique to measure the coherence length is to analyse the momentum distribution along the long direction of the condensate. Our measurement is based on four-photon velocity-selective Bragg diffraction. Atoms are diffracted out of the condensate by interaction with a moving standing wave, formed by two counter-propagating laser beams with a relative detuning  $\delta$  [13,26]. Due to the Doppler effect, the momentum component resonantly diffracted out of the condensate is  $p_z = M(\delta - 8\omega_R)/(2k_L)$  with  $\omega_R = \hbar k_L^2/(2M)$ ,  $M$  the atomic mass, and  $k_L = 2\pi/\lambda$  ( $\lambda = 780.2$  nm). The predicted spectral width is therefore  $\alpha\Delta\nu_\phi$ , where

$$\Delta\nu_\phi = \frac{2\hbar k_L}{2\pi M L_\phi}. \quad (4.2)$$

To build the momentum spectrum of the quasi-condensate, we measure the fraction of diffracted atoms versus the detuning  $\delta$  between the counter-propagating laser beams. The differential frequency  $\delta$  must be stable to better than the desired spectral resolution, about 200 Hz for our typical  $L_\phi = 10 \mu\text{m}$ . The optical setup is as follows. A single laser beam is spatially filtered by a fiber optic, separated into two arms with orthogonal polarizations, frequency shifted by two independent 80 MHz acousto-optic modulators, and recombined. The modulators are driven by two synthesizers stable to better than 1 Hz over the typical acquisition time of a spectrum. The overlapping, recombined beams are then sent through the vacuum cell, parallel (to within 1 mrad) to the long axis of the trap, and retro-reflected to obtain two standing waves with orthogonal polarizations, moving in opposite directions. The lasers are tuned 6.6 GHz below resonance to avoid Rayleigh scattering. The laser intensities (about 2 mW/cm<sup>2</sup>) are adjusted to keep the diffraction efficiency below 20 %.

Bragg spectra have been taken at various temperatures between 90(10) nK and 350(20) nK, while  $T_c$  varied from 280(15) nK to 380(20) nK. The temperature was fixed to within 20 nK by controlling the final trap depth to a precision of 2 kHz. The line shape of the spectra is clearly Lorentzian, not Gaussian (see Fig. 2). This is a significant result, because a Lorentzian-like profile is expected for a momentum distribution dominated by phase fluctuations (see [12]), in contrast to the gaussian-like profile expected for a pure condensate [27,13]. From the Lorentzian fit, we extract the measured half-width  $\Delta\nu_M$  for each temperature.

Figure 3 shows the measured spectral width  $\Delta\nu_M$  versus  $\Delta\nu_\phi$ . Dispersion of the measured  $n_1(0)$  and  $T$  results in the horizontal error bars on  $\Delta\nu_\phi$ , while vertical error bars indicate the standard deviation of the fit width. We assume that all experimental broadenings result in a Gaussian apparatus function of half-width  $w_G$ , to be convolved by the Lorentzian momentum

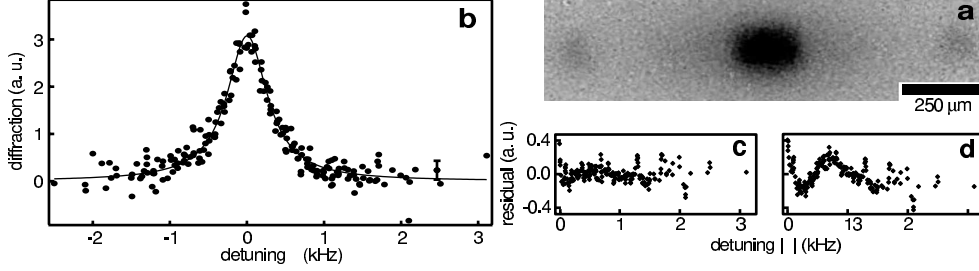


**Fig. 2.** (a) Absorption image of degenerate cloud (center) and diffracted atoms (left and right), averaged over several shots, after free-flight expansion. (b) Diffraction efficiency (rescaled) versus relative detuning of the Bragg lasers at  $T = 261(13)$  nK, corresponding to  $T/T_\phi = 20(2)$ . A typical statistical error bar is shown. This spectrum is the superposition of 12 “elementary spectra”, as described in the text. The true average center is  $30.18(2)$  kHz, close to  $30.17$  kHz, the four-photon recoil frequency. The solid line is a Lorentzian fit, giving a half-width at half-maximum (HWHM) of  $316(10)$  Hz. (c) and (d) show respectively the residual of a Lorentzian and of a Gaussian fit to the above spectrum. Residuals are folded around the  $\delta = 0$  axis, and smoothed with a six-point-wide sliding average.

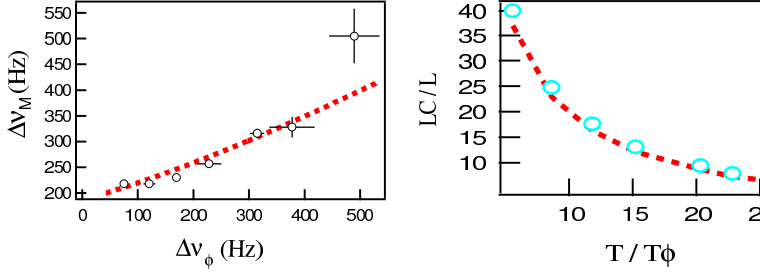


**Fig. 3.** Left : Half-widths at half-maximum  $\Delta\nu_M$  of the experimental Bragg spectra versus the parameter  $\Delta\nu_\phi \propto \hbar/L_\phi$  (see text). Vertical error bars are the standard deviations of the fit width; the horizontal error bars are the one-sigma statistical dispersions of  $\Delta\nu_\phi$ . The solid line is a fit assuming a Voigt profile for the spectra. Right : coherence length deduced from the width, after correction for the gaussian broadening,

profile with a half-width  $\alpha\Delta\nu_\phi$ . The convolution, a Voigt profile, has a half-width  $\alpha\Delta\nu_\phi/2 + \sqrt{w_G^2 + (\alpha\Delta\nu_\phi)^2/4}$ . Note that fitting a Voigt profile instead of a Lorentzian to a spectrum gives the same total HWHM to less than 5 %, but the Lorentzian shape is too predominant to extract reliably the Gaussian and the Lorentzian contributions to the profile. Using  $\alpha$  and  $w_G$  as free parameters to fit the data of Fig. 3, we find  $w_G = 176(6)$  Hz, and  $\alpha = 0.64(5)(5)$ . The first uncertainty quoted for  $\alpha$  is the standard deviation of the fit value. The second results from calibration uncertainties on the magnification of the imaging system and on the total atom number, which do not affect  $w_G$ . The agreement of the measured value of  $\alpha$  with the theoretical value 0.67, to within the 15 % experimental uncertainty, confirms quantitatively the temperature dependence of the momentum width predicted in Ref. [5]. The coherence length  $\hbar/p_\phi$  deduced from this measurement varies between  $5.9(8)$  and  $39(4)$   $\mu\text{m}$ , in the range  $6 < T/T_\phi < 28$ .

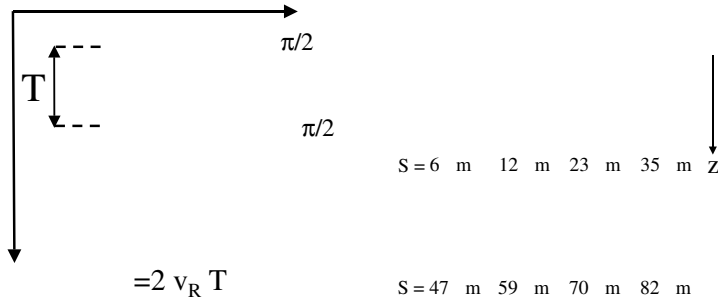


**Fig. 4.** Left : The atom interferometer used for our coherence length measurement uses  $2 \pi/2$  pulse to create and overlap 2 displaced copies of the same condensate. Right : The fringe spacing and contrast changes as the time between the 2 pulses (i.e. the separation between the 2 copies) is changed. A measurement of the fringe contrast directly measures the spatial first-order correlation function of the matter-wave field.

## 4.2 Interferometry with elongated BECs

The Bragg spectroscopy method has proven to be appropriate for measuring short coherence lengths. However, when applied to nearly coherent condensates ( $L_C \sim L$ ), the extremely narrow Bragg resonance becomes increasingly difficult to resolve (for  $L_\Phi \sim 40 \mu\text{m}$ , the momentum width is already of the order of our resolution). However, since our goal is to investigate the cross-over from a phase coherent to a phase-fluctuating condensate, we need to measure coherence length larger than the  $39(4) \mu\text{m}$  attainable with Bragg spectroscopy. For this, we have implemented a matter-wave interferometer [9]. As shown on figure 4, this interferometer uses a first  $\frac{\pi}{2}$  bragg pulse to split the condensate in 2 equal copies that fly apart from each other at a velocity  $2v_R = 2 \frac{\hbar k}{M} \simeq 1.2 \text{ cm/s}$ . After a time of flight  $2\text{ms} < T < 10\text{ms}$ , the 2 copies, that separate by  $2v_R \times T$ , are recombined using a second  $\frac{\pi}{2}$  pulse, that creates 2 interferometer output (see fig. 4). For finite  $T$ , complementary fringes appear in the two output ports, because of the smoothly varying expansion phase that results from the conversion of a small fraction of the initial mean-field energy ( $\sim \epsilon^2 \mu$ ) into axial kinetic energy. The resulting fringe pattern is Fourier analyzed to find the contrast and the fringe spacing in reciprocal space. In this way, we filter out shot-to-shot, global phase fluctuations that would result in a translation of the fringe pattern as a whole. This method allows for averaging many processed images without artificially reducing the contrast. After this processing, this method allows a direct measure-

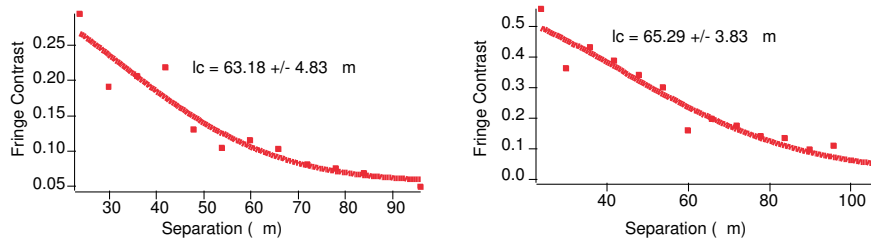


**Fig. 5.** Example of 2 direct measurements of the correlation function (fringe contrast) as a function of the separation  $s$  between the two copies of the condensate ; left :  $T_\Phi/T = 0.45$  and  $2 \times 10^5$  atoms ( $L_{\text{TF}} \sim 100 \mu\text{m}$ ), right :  $T_\Phi/T = 0.75$  and  $1.3 \times 10^5$  atoms ( $L_{\text{TF}} \sim 90 \mu\text{m}$ )

ment of the correlation function  $\mathcal{C}^{(1)}$  as a function of separation  $s$  (see figure 5), irrespective of the amount of phase fluctuations.

## 5 CONCLUSION

We have demonstrated two important features of elongated Bose-Einstein condensates: (i) the dimension of the condensate after expansion; (ii) the momentum distribution of quasicondensates; Our method, along with atom interferometry can be applied to investigate how long range order develops during the condensate growth.

## References

- [1] A. Görlitz, J. M. Vogels, A. E. Leanhardt, C. Raman, T. L. Gustavson, J. R. Abo-Shaeer, A. P. Chikkatur, S. Gupta, S. Inouye, T. Rosenband, and W. Ketterle, *Phys. Rev. Lett.* **87**, 130402 (2001).
- [2] F. Schreck, L. Khaykovich, K. L. Corwin, G. Ferrari, T. Bourdel, J. Cubizolles, and C. Salomon *Phys. Rev. Lett.* **87**, 080403 (2001).
- [3] M. Greiner, I. Bloch, O. Mandel, T. W. Hänsch, and T. Esslinger, *Phys. Rev. Lett.* **87**, 160405 (2001).
- [4] D. S. Petrov, G. V. Shlyapnikov, and J. T. M. Walraven, *Phys. Rev. Lett.* **85**, 3745 (2000).
- [5] D. S. Petrov, G. V. Shlyapnikov, and J. T. M. Walraven, *Phys. Rev. Lett.* **87**, 050404 (2001).
- [6] S. Dettmer, D. Hellweg, P. Ryytty, J. J. Arlt, W. Ertmer, K. Sengstock, D. S. Petrov, G. V. Shlyapnikov, H. Kreutzmann, L. Santos, and M. Lewenstein, *Phys. Rev. Lett.* **87**, 160406 (2001).
- [7] D. Hellweg, S. Dettmer, P. Ryytty, J. J. Arlt, W. Ertmer, K. Sengstock, D. S. Petrov, G. V. Shlyapnikov, H. Kreutzmann, L. Santos, and M. Lewenstein, *Appl. Phys. B* **73**, 781 (2001).
- [8] I. Shvarchuk *et al.*, *Phys. Rev. Lett.* **89**, 270404 (2002).
- [9] D. Hellweg, L. Cacciapiuoti, M. Kottke, T. Schulte, K. Sengstock, W. Ertmer, J. J. Arlt *cond-mat/0303308*, *Phys. Rev. Lett.* **91**, 010406 (2003).
- [10] S. Richard *et al.*, *cond-mat/0303137*, *Phys. Rev. Lett.* **91**, 010405 (2003).
- [11] F. Gerbier *et al.*, *cond-mat/0210206*.
- [12] F. Gerbier *et al.*, *Phys. Rev. A* **67**, 051602 (2003).
- [13] J. Stenger, S. Inouye, A. P. Chikkatur, D. M. Stamper-Kurn, D. E. Pritchard, and W. Ketterle, *Phys. Rev. Lett.* **82**, 4569 (1999).
- [14] B. Desruelle *et al.*, *Phys. Rev. A* **60**, R1759 (1999).
- [15] V. Boyer, thèse de doctorat 2000
- [16] The atom number measurement is calibrated to a 20 % precision by comparing a measurement of  $N_c$  to theory [17].
- [17] F. Dalfovo, S. Giorgini, L. P. Pitaevskii, S. Stringari, *Rev. Mod. Phys.* **71**, 463 (1999).
- [18] E. G. M. van Kempen, S. J. J. M. F. Kokkelmans, D. J. Heinzen, B. J. Verhaar, *Phys. Rev. Lett.* **88**, 093201 (2002).
- [19] Y. Castin, R. Dum, *Phys. Rev. Lett.* **77**, 5315 (1996); Yu. Kagan, E. L. Surkov, G. V. Shlyapnikov, *Phys. Rev. A* **55**, R18 (1997).
- [20] V. V. Goldman, I. F. Silvera, A. J. Leggett, *Phys. Rev. B* **24**, 2870 (1981); S. Giorgini, L. P. Pitaevskii, S. Stringari, *J. Low Temp. Phys.* **109**, 309 (1997).
- [21] A. L. Zubarev, Y. E. Kim, *Phys. Rev. A* **65**, 035601 (2002).
- [22] E. W. Hagley, L. Deng, M. Kozuma, M. Trippenbach, Y. B. Band, M. Edwards, M. Doery, P. S. Julienne, K. Helmerson, S. L. Rolston, and W. D. Phillips, *Phys. Rev. Lett.* **83**, 3112 (1999).
- [23] J. W. Kane, L. P. Kadanoff, *Phys. Rev.* **155**, 80 (1967).
- [24] Using the relevant expressions for  $n_1(0)$ , the results obtained in [4] for the 1D case and [5] for the 3D case are recovered, in the limit  $L_\phi \ll L$ .
- [25] The coefficient  $\alpha$  accounts for the density profile, but varies little with the exact form of  $n_1$ : for instance  $\alpha = 0.64$  in the 1D TF limit, and  $\alpha = 0.5$  for a uniform profile.
- [26] J. Steinhauer, R. Ozeri, N. Katz, N. Davidson, *Phys. Rev. Lett.* **88**, 120407 (2002).
- [27] F. Zambelli, L. Pitaevskii, D. M. Stamper-Kurn, and S. Stringari, *Phys. Rev. A* **61**, 063608 (2000).